



Lead-free halide perovskite hollow nanospheres to boost photocatalytic activity for CO₂ reduction

Yan-Fei Mu ^{a,b,1}, Jin-Shuang Zhao ^{a,1}, Li-Yuan Wu ^a, Ke-Ying Tao ^a, Zhao-Lei Liu ^a, Fu-Quan Bai ^c, Di-Chang Zhong ^{a,*}, Min Zhang ^{a,*}, Tong-Bu Lu ^{a,*}

^a MOE International Joint Laboratory of Materials Microstructure, Institute for New Energy Materials and Low Carbon Technologies, School of Materials Science and Engineering, Tianjin University of Technology, Tianjin 300384, China

^b School of Chemistry and Chemical Engineering, Yangzhou University, Yangzhou 225009, Jiangsu, China

^c Institute of Theoretical Chemistry, College of Chemistry, Jilin University, Changchun 130012, China



ARTICLE INFO

Keywords:

Lead-free perovskite
Hollow nanospheres
CO₂ reduction
Cs₃Sb₂Br₉
Dinuclear metal complex

ABSTRACT

Strong photoresponse, efficient charge separation, and high surface activity are three important requirements for an ideal photocatalyst, while few photocatalysts can fully meet these requirements. Herein, we report such a photocatalyst based on lead-free halide perovskite hollow nanospheres (H-Cs₃Sb₂Br₉) by a facile antisolvent-assisted method. The hollow structure of H-Cs₃Sb₂Br₉ improves the light-harvesting performance; The formation of surface shallow trap states contributes to promoting the excited-carrier separation; The ligand-free termination surface of H-Cs₃Sb₂Br₉ facilitates the exposure of Br vacancies and active sites, thus strengthens the CO₂ adsorption and accelerates surface reactivity dynamics. As a result, with a dinuclear Co(II) complex as the co-catalyst, H-Cs₃Sb₂Br₉ exhibits a record-high photocatalytic activity for CO₂ reduction, with a CO yield of 15,010.4 ± 550.4 μmol g⁻¹ after 8 h of illumination under simulated solar light (100 mW cm⁻²). This research presents a new way to develop cost-effective photocatalysts for CO₂ reduction.

1. Introduction

Photocatalytic CO₂ reduction into fuels and value-added chemicals is widely regarded as a highly promising approach to achieving carbon neutralization [1]. The key to its success lies in the development of cost-effective and highly efficient photocatalysts [2,3]. It is well-known that ideal photocatalysts should generally possess three key features, namely strong photoresponse, efficient charge separation, and high surface activity. A series of semiconductor photocatalysts have been designed based on these features and used for photocatalytic CO₂ reduction [4–9]. Also, several strategies including regulation of crystal plane, engineering of strain, construction of heterojunction, the introduction of defect, etc. have been employed to improve the photocatalytic activity for CO₂ reduction [10–17]. However, it was found that all these efforts are placed on the improvement of one or two of the three key features. It can be anticipated that the simultaneous presence of these three key features in a photocatalyst would lead to a notable breakthrough in enhancing the photocatalytic activity for CO₂ reduction.

Metal halide perovskites (MHPs), as a type of low-cost semiconductor material, exhibit great potential in photocatalytic CO₂ reduction owing to their excellent light absorption ability, long photo-generated carrier diffusion length, tunable bandgaps, among other advantages [18–20]. In particular, lead-free MHPs, friendly to the environment and possessing good stability, have received more attention in recent years [21–25]. However, lead-free MHPs usually have a low structure and electronic dimensionality at the molecular level, which increases the carrier mass and the exciton-phonon interaction, causing the recombination of electron-hole and the reduction of carrier lifetime [26–28]. Lead-free MHPs thus suffer from poor photoelectric properties and low efficiency in photocatalytic CO₂ reduction [29,30]. In addition, MHPs-based nanocrystal photocatalysts usually need to be protected by end-capping long-chain organic ligands, to prevent them from aggregation. Clearly, this will result in reduced exposure of catalytic active sites on the surface of MHPs nanocrystals, consequently leading to a decrease in the photocatalytic efficiency for CO₂ reduction. Based on the above analyses, it is reasonably concluded that the preparation of MHPs nanocrystals with porous nanostructures and without surface ligands

* Corresponding authors.

E-mail addresses: dczhong@email.tjut.edu.cn (D.-C. Zhong), zm2016@email.tjut.edu.cn (M. Zhang), lutongbu@tjut.edu.cn (T.-B. Lu).

¹ These authors contributed equally to this work.

would improve the photocatalytic CO_2 reduction activity. The porous structure without surface ligands will endow the MHPs nanocrystals with large surface area and rich exposed active sites. Meantime, without surface ligands will lead to the possible formation of shallow traps on the MHPs surface due to the halide vacancy, which contributes to capturing photogenerated electrons, thus facilitating charge separation and extending the excited state lifetime [31–33]. Along with this research proposal, we devoted to developing porous MHPs nanocrystals without surface ligands, aiming at obtaining efficient photocatalysts for CO_2 reduction.

In this work, we report a ligand-free MHPs hollow nanosphere with extremely high efficiency for photocatalytic CO_2 reduction. This MHPs hollow nanosphere was obtained by injection of a DMSO solution containing CsBr and SbBr_3 into an anti-solvent of methyl acetate with stirring. The afforded hollow $\text{Cs}_3\text{Sb}_2\text{Br}_9$ nanosphere ($\text{H-}\text{Cs}_3\text{Sb}_2\text{Br}_9$) possesses stronger light absorption, larger specific surface area, and improved carrier separation compared with the $\text{Cs}_3\text{Sb}_2\text{Br}_9$ nanocrystals ($\text{N-}\text{Cs}_3\text{Sb}_2\text{Br}_9$) traditionally prepared. Moreover, the ligand-free surface with rich Br vacancies can enable the $\text{H-}\text{Cs}_3\text{Sb}_2\text{Br}_9$ to expose abundantly accessible active sites and promote the electronic transfer among $\text{H-}\text{Cs}_3\text{Sb}_2\text{Br}_9$, CO_2 , and cocatalyst. As a result, $\text{H-}\text{Cs}_3\text{Sb}_2\text{Br}_9$ demonstrates a yield of $5059.7 \pm 169.6 \mu\text{mol g}^{-1}$ for photocatalytic CO_2 reduction to CO , almost 13 folds over that of $\text{N-}\text{Cs}_3\text{Sb}_2\text{Br}_9$. With a dinuclear cobalt(II) molecular complex as a cocatalyst, an unprecedented photocatalytic CO_2 -to- CO conversion activity can be obtained, with the CO yield of $15,010.4 \pm 550.4 \mu\text{mol g}^{-1}$ after being illuminated by simulated solar light (100 mW cm^{-2}) for 8 h, over 28 folds higher than that of traditional $\text{N-}\text{Cs}_3\text{Sb}_2\text{Br}_9$.

2. Experimental section

2.1. Materials

Cesium bromide (CsBr , 99.5%) and antimony (III) bromide (SbBr_3 , 99.5%) were purchased from Xi'an Polymer Light Technology Corporation. Oleic acid (90%), methyl acetate (98%), cesium carbonate (Cs_2CO_3 , 99.99%), octanoic acid (98%), tetrabutylammonium chloride ($\text{C}_{16}\text{H}_{36}\text{NCl}$), and dimethyl sulfoxide (DMSO, HPLC, >99.9%) were purchased from Aladdin. Methanol (HPLC, 99.9%), 1-octadecene (90%), oleylamine (80–90%), and $^{13}\text{CH}_3\text{OH}$ were purchased from Sigma-Aldrich. Trichloromethane (CHCl_3) was purchased from China National Pharmaceutical Group Corporation. $^{13}\text{CO}_2$ and H_2^{18}O were purchased from Energy Chemical. All of the reagents were commercially available and used without further purification.

2.2. Sample preparation

Preparation of Cs -oleate. Cs_2CO_3 (162.9 mg), 1-octadecene (4.0 mL), and oleic acid (0.5 mL) were mixed in a three-necked flask. The mixture was degassed by vacuum and kept at 120 °C for 1 h. Then the reaction was heated up to 150 °C under Ar flow and stirred vigorously for 3 h until the solution was clarified. The resulting product was cooled to room temperature for the next step.

Synthesis of $\text{Cs}_3\text{Sb}_2\text{Br}_9$ nanocrystals ($\text{N-}\text{Cs}_3\text{Sb}_2\text{Br}_9$). SbBr_3 (36.1 mg), 1-octadecene (10.0 mL), oleylamine (0.4 mL), and octanoic acid (1.0 mL) were mixed in a three-neck flask, and degassed by vacuum at 80 °C for 1 h. Then it was heated up to 180 °C under Ar flow, and the prepared Cs -oleate solution (0.3 mL) was rapidly injected into the reaction solution. After 60 s, the reaction mixture was cooled down with liquid nitrogen. The final solution was centrifuged at 7800 rpm/min for 3 min to extract the precipitates. The $\text{N-}\text{Cs}_3\text{Sb}_2\text{Br}_9$ powder can be obtained after washing three times with hexane and drying for 6 h at 60 °C. In addition, $\text{N-}\text{Cs}_3\text{Sb}_2\text{Br}_9$ -220 can be prepared by changing the injection temperature from 180 °C to 200 °C.

Synthesis of ligand-free $\text{Cs}_3\text{Sb}_2\text{Br}_9$ hollow nanospheres ($\text{H-}\text{Cs}_3\text{Sb}_2\text{Br}_9$). CsBr (46.9 mg) and SbBr_3 (53.1 mg) were added in DMSO

(0.5 mL) followed by stirring for 20 min until the mixture completely dissolved to gain the precursor solution. Subsequently, the prepared precursor solution (500 μL) was rapidly injected into the anti-solvent (methyl acetate, 25 mL) followed by stirring for 10 min. The resulting solution was centrifuged and washed with toluene three times successively, and thereafter annealed in an oven at 150 °C for 6 h to obtain $\text{H-}\text{Cs}_3\text{Sb}_2\text{Br}_9$ nanospheres.

Synthesis of $[\text{Co}_2(\text{OH})\text{L}^1](\text{ClO}_4)_3$ (Co_2L). Co_2L was synthesized as described in our previous work [34].

Synthesis of $\text{Co}_2\text{L-H-}\text{Cs}_3\text{Sb}_2\text{Br}_9$ composite photocatalyst. 5 mg of as-prepared $\text{H-}\text{Cs}_3\text{Sb}_2\text{Br}_9$ nanospheres were added in 5 mL acetonitrile solution and dispersed evenly by ultrasound. Then 320 mL of dinuclear cobalt acetonitrile solution (6 mM) was added to the above solution, and stirred under dark conditions for 2 h, followed by centrifuging with 5000 rpm/min for 5 min. The resulting precipitation was the composite catalyst. Besides, the $\text{Co}_2\text{L-N-}\text{Cs}_3\text{Sb}_2\text{Br}_9$ composite was prepared in the same way by using $\text{N-}\text{Cs}_3\text{Sb}_2\text{Br}_9$ instead of $\text{H-}\text{Cs}_3\text{Sb}_2\text{Br}_9$.

2.3. In-situ irradiated X-ray photoelectron spectroscopy (ISI-XPS)

ISI-XPS measurements were performed with an ESCALAB250Xi X-ray photoelectron spectrometer. A Xe-lamp (300 W) with a UVICUT400 filter was used as the bias light source. The bias light source was set ~ 40 cm away from the sample stage.

2.4. In-situ Raman spectroscopy

In situ Raman spectroscopy was measured on a HORIBA Jobin Yvon's high-resolution laser confocal micro-Raman spectrometer which is equipped with an aberration-corrected Czerny Turner total reflection spectrometer (focal length 800 mm). Argon ion laser with an excitation wavelength of 532 nm was used as the excitation source. Laser power was set to 100%, and the test range was $600 - 1800 \text{ cm}^{-1}$. Oxygen was used as the electron capture agent.

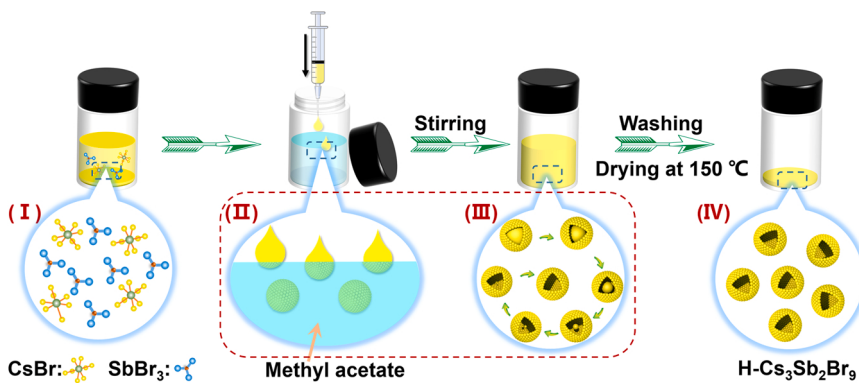
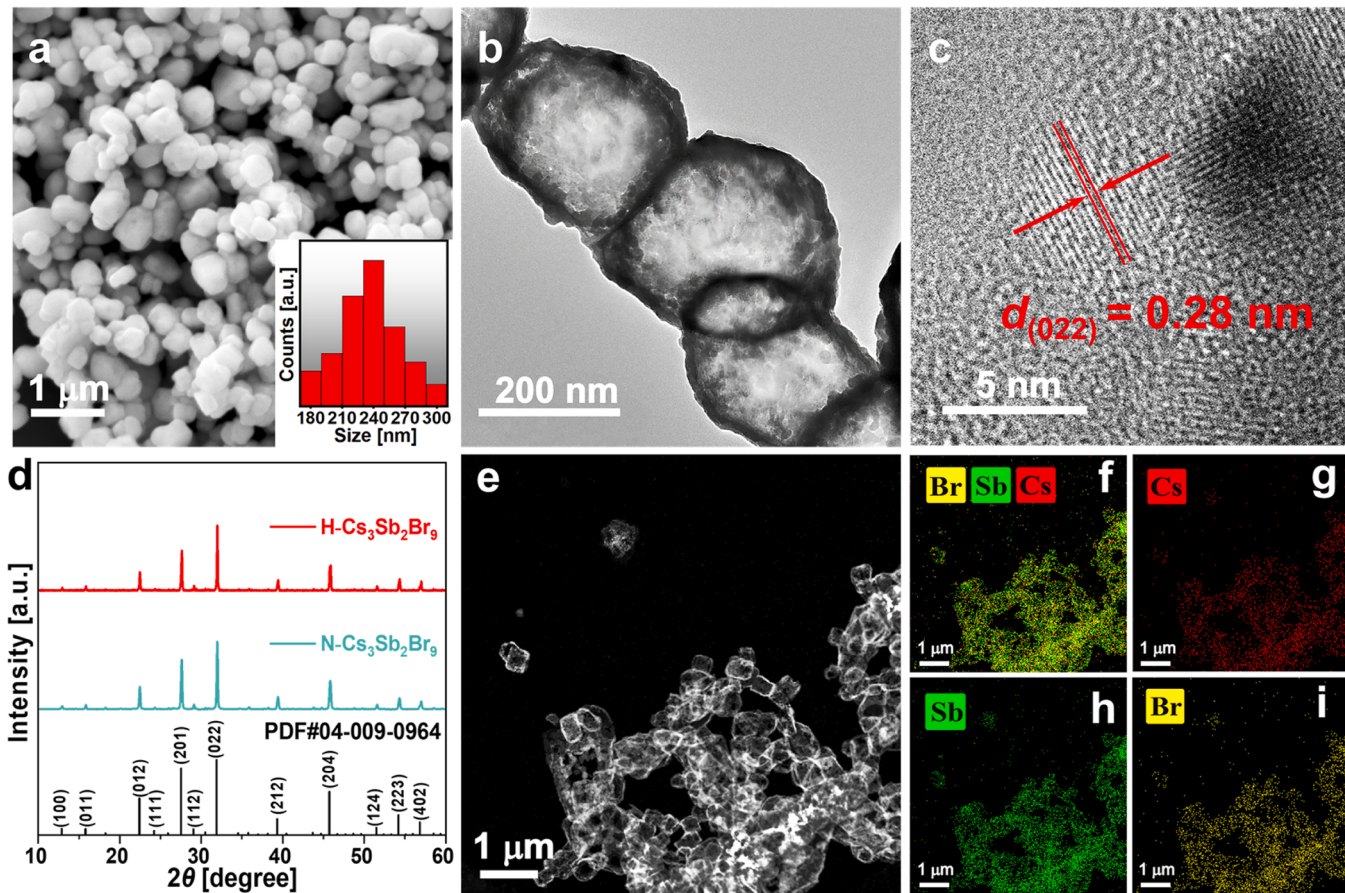
2.5. Photocatalytic experiments

All the CO_2 reduction reactions were performed in a gas-solid reaction system. 50 μL H_2O and 50 μL CH_3OH were injected into the reaction system as the electron source. 2 mg of sample was added into the reaction system as the photocatalyst. The reaction system was degassed to remove O_2 and import CO_2 for 20 min. Solar illumination was simulated using a 300 W Xenon lamp (Cell-HXF300, CEAULICHT) equipped with a UVVISCUT400 filter, and the light intensity was adjusted to 100 mW cm^{-2} by NREL-calibrated silicon solar cell. The gas products were analyzed by the SHIMADZU GC-2014 gas chromatograph instrument equipped with TCD and FID dual detectors. The amount of formic acid was measured by ion chromatography (IC) manufactured by Vantone Inc.

3. Results and discussion

3.1. Preparation and structure of $\text{H-}\text{Cs}_3\text{Sb}_2\text{Br}_9$

The $\text{H-}\text{Cs}_3\text{Sb}_2\text{Br}_9$ nanospheres were constructed through a facile antisolvent-assisted method (Fig. 1). Briefly, a precursor solution was first prepared by dissolving a certain amount of CsBr and SbBr_3 in dimethyl sulfoxide (DMSO). Then the precursor DMSO solution was rapidly injected into an anti-solvent of methyl acetate with stirring. Due to the effect of antisolvent, the $\text{H-}\text{Cs}_3\text{Sb}_2\text{Br}_9$ nanospheres can be obtained by in-situ sequential crystallization of precursor droplets from outside to inside. The scanning electron microscopy (SEM) measurement demonstrated that $\text{H-}\text{Cs}_3\text{Sb}_2\text{Br}_9$ was an irregular nanosphere with an average size of $\sim 220 \text{ nm}$ (Fig. 2a). The transmission electron microscopy (TEM) image confirmed that $\text{H-}\text{Cs}_3\text{Sb}_2\text{Br}_9$ exhibited a clear hollow nanostructure (Fig. 2b). In the high-resolution TEM image of $\text{H-}\text{Cs}_3\text{Sb}_2\text{Br}_9$

Fig. 1. The growth process for H-Cs₃Sb₂Br₉.Fig. 2. (a–c) SEM, TEM, and HRTEM images of H-Cs₃Sb₂Br₉. (d) XRD patterns of H-Cs₃Sb₂Br₉ and N-Cs₃Sb₂Br₉. (e–i) TEM and corresponding EDS images of H-Cs₃Sb₂Br₉.

Cs₃Sb₂Br₉ (Fig. 2c), the well-defined lattice spacings of Cs₃Sb₂Br₉ (0.28 nm) can be identified, corresponding to the (022) lattice planes of hexagonal-phase Cs₃Sb₂Br₉. The X-ray diffraction (XRD) patterns (Fig. 2d) further clarified that the as-prepared H-Cs₃Sb₂Br₉ can be indexed to P-3m1(164) hexagonal space group (PDF card no. 04-009-0964), with high crystallinity characteristic of strong diffraction peaks at 22.4°, 27.5°, 31.9°, 39.3°, and 45.7°, matching well with the (012), (201), (022), (212), and (204) facets, respectively. Additionally, further TEM (Fig. 2e) and corresponding energy-dispersive X-ray spectroscopy (EDS) elemental mapping measurements (Fig. 2f–i) demonstrated a homogeneous distribution for Cs, Sb, and Br elements in H-Cs₃Sb₂Br₉. The presented light color interior cavity and dark color shell further confirmed the hollow nanostructure of H-Cs₃Sb₂Br₉. For

comparison, the traditional ligand-terminated Cs₃Sb₂Br₉ nanocrystals (N-Cs₃Sb₂Br₉) with an average size of 24 nm were also prepared by a hot-injection method (Fig. S1) [35], which also exhibited hexagonal-phase structure with high crystallinity (Fig. 2d).

To verify the formation mechanism of H-Cs₃Sb₂Br₉ nanospheres, control experiments have been performed at different growth stages of Cs₃Sb₂Br₉. As presented in Fig. S2, when the growth was stopped in the initial stage (10 s), the resulting Cs₃Sb₂Br₉ exhibited a solid nanosphere. With the extension of growth time, the inner core gradually disappeared, and the solid nanosphere finally transformed into a hollow nanostructure. The corresponding X-ray diffraction (XRD) patterns of samples (Fig. S3) revealed that the crystallinity of Cs₃Sb₂Br₉ became better with the prolongation of growth time, showing gradually enhanced

intensities of characteristic peaks. Overall, the precursor droplets undergo an in-situ crystallization transformation process due to the effect of antisolvent. As the precursor droplets were rapidly injected into the anti-solvent, the outer layer of the $\text{Cs}_3\text{Sb}_2\text{Br}_9$ droplet nucleated and crystallized rapidly to form an outer spherical shell due to the anti-solvent effect (II) in Fig. 1. The formation of the outer spherical shell can slow down the mixing of DMSO in droplets and the anti-solvent methyl acetate, which conduces to the formation of hollow nanostructures. As visualized in Fig. 1 (III and IV), the inner precursor underwent slow infiltration and crystallization, eventually forming hollow nanostructures.

3.2. Thermodynamic and CO_2 uptake properties

To explore the potential of $\text{H-Cs}_3\text{Sb}_2\text{Br}_9$ for photocatalytic CO_2 reduction, we first studied and compared the structure-dependent light-

harvesting and thermodynamics properties of $\text{H-Cs}_3\text{Sb}_2\text{Br}_9$ and $\text{N-Cs}_3\text{Sb}_2\text{Br}_9$, by combined UV–Vis diffuse reflectance spectra (UV–Vis DRS) and ultraviolet photoelectron spectra (UPS). As depicted in Fig. 3a, both $\text{H-Cs}_3\text{Sb}_2\text{Br}_9$ and $\text{N-Cs}_3\text{Sb}_2\text{Br}_9$ exhibited strong light absorption in the visible region with a similar photoresponse onset wavelength of ~ 525 nm. It was noted that an appreciably enhanced light-harvesting was obtained for $\text{H-Cs}_3\text{Sb}_2\text{Br}_9$ compared with $\text{N-Cs}_3\text{Sb}_2\text{Br}_9$, due to the multiple reflections of incident light in the cavity of the hollow nanostructure [36]. The band-gaps (E_g) of $\text{H-Cs}_3\text{Sb}_2\text{Br}_9$ and $\text{N-Cs}_3\text{Sb}_2\text{Br}_9$ can be calculated via the Tauc plots (inset of Fig. 3a) derived from UV–Vis DRS spectra, both being 2.46 eV. To determine the band structures of $\text{H-Cs}_3\text{Sb}_2\text{Br}_9$ and $\text{N-Cs}_3\text{Sb}_2\text{Br}_9$, we analyzed the onset edge (E_i) and the secondary electron cutoff (E_{cutoff}) positions of UPS spectra (Fig. 3b). The valence band edge potential (E_{VB}) can be obtained according to the equation $E_{\text{VB}} = 21.22 - (E_{\text{cutoff}} - E_i)$, being 2.07 and 1.97 V for $\text{H-Cs}_3\text{Sb}_2\text{Br}_9$ and $\text{N-Cs}_3\text{Sb}_2\text{Br}_9$, respectively, versus the standard

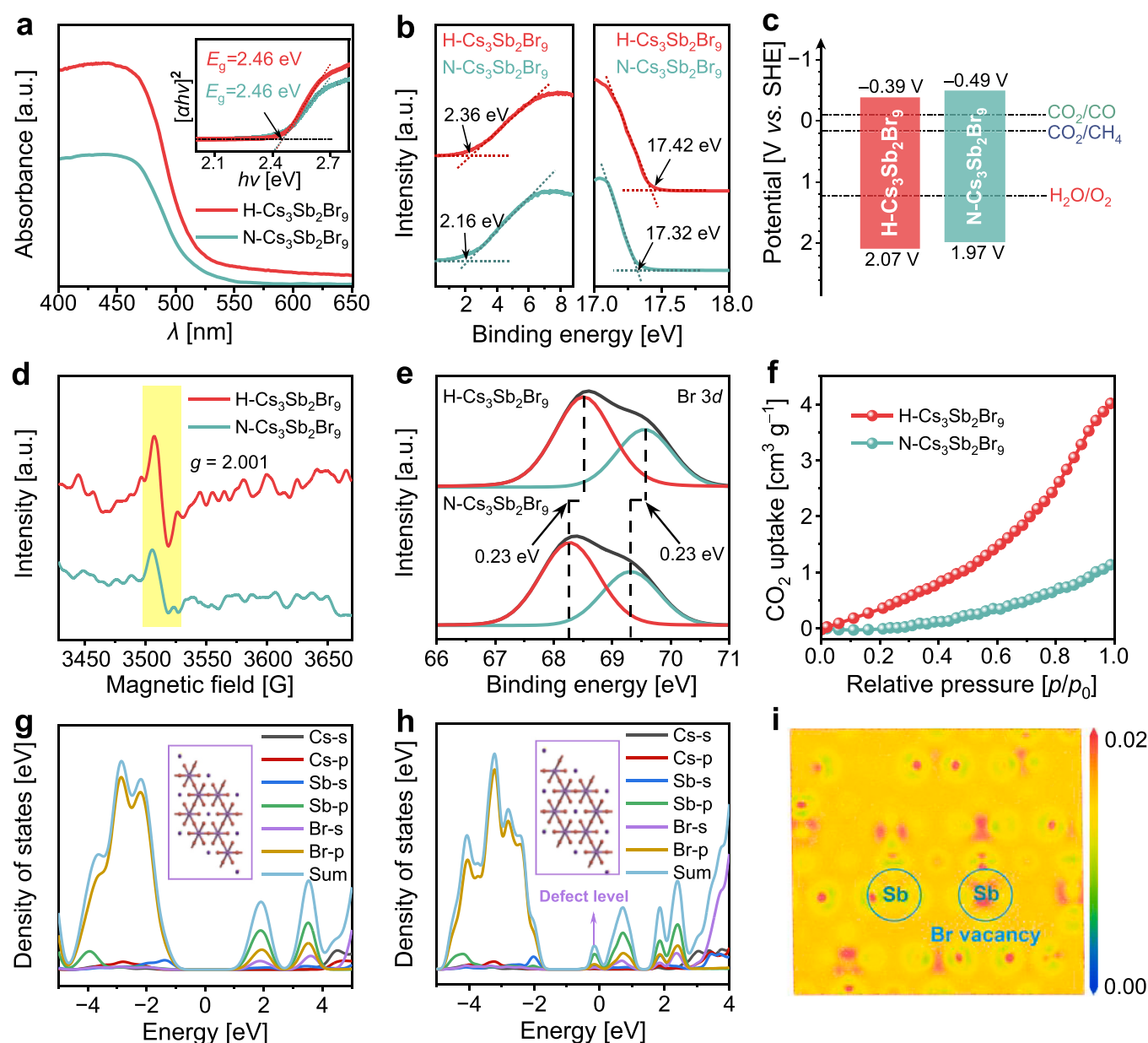


Fig. 3. (a) UV–Vis DRS spectra of $\text{H-Cs}_3\text{Sb}_2\text{Br}_9$ and $\text{N-Cs}_3\text{Sb}_2\text{Br}_9$. The insert shows the corresponding Tauc plots. (b) UPS spectra of $\text{H-Cs}_3\text{Sb}_2\text{Br}_9$ and $\text{N-Cs}_3\text{Sb}_2\text{Br}_9$. (c) Schematic illustration of $\text{H-Cs}_3\text{Sb}_2\text{Br}_9$ and $\text{N-Cs}_3\text{Sb}_2\text{Br}_9$ band structures derived from the UPS spectra and UV–Vis DRS spectra. (d) ESR spectra of $\text{H-Cs}_3\text{Sb}_2\text{Br}_9$ and $\text{N-Cs}_3\text{Sb}_2\text{Br}_9$. (e) High-resolution XPS spectra for Br 3d in $\text{H-Cs}_3\text{Sb}_2\text{Br}_9$ and $\text{N-Cs}_3\text{Sb}_2\text{Br}_9$. (f) CO_2 uptake curve of $\text{H-Cs}_3\text{Sb}_2\text{Br}_9$ and $\text{N-Cs}_3\text{Sb}_2\text{Br}_9$. (g, h) Partial density of states (PDOS) for $\text{N-Cs}_3\text{Sb}_2\text{Br}_9$ and $\text{H-Cs}_3\text{Sb}_2\text{Br}_9$. (i) Localized charge density distribution of $\text{H-Cs}_3\text{Sb}_2\text{Br}_9$ on (022) surface, plotted from 0 (blue) to 0.02 $\text{e } \text{\AA}^{-3}$ (red).

hydrogen electrode (vs. SHE). Based on the values of E_g and E_{VB} , the corresponding conduction band edge potentials (E_{CB}) can be determined to be -0.39 and -0.49 V (vs. SHE) for H-Cs₃Sb₂Br₉ and N-Cs₃Sb₂Br₉, respectively. The band structures of H-Cs₃Sb₂Br₉ and N-Cs₃Sb₂Br₉ have been presented in Fig. 3c. It was revealed that the photogenerated electrons in both H-Cs₃Sb₂Br₉ and N-Cs₃Sb₂Br₉ possess sufficient driving force for the photoreduction of CO₂ into value-added chemicals, such as CO (-0.12 V vs. SHE) and CH₄ (0.17 V vs. SHE) et al. The E_{VB} and E_{CB} for H-Cs₃Sb₂Br₉ move positively relative to that of N-Cs₃Sb₂Br₉, probably due to the absence of ligand passivation on H-Cs₃Sb₂Br₉ generating generous surface defects and changing the electronic structure [37]. The positive shift of the E_{VB} position is conducive to the improvement of the driving force for the oxidation reaction [38,39].

The electron spin resonance (ESR) spectra shown in Fig. 3d presented a clear signal at $g = 2.001$, confirming that the surface defects for both H-Cs₃Sb₂Br₉ and N-Cs₃Sb₂Br₉ resulted from the Br vacancy [40]. It was noted that H-Cs₃Sb₂Br₉ displayed an enhanced ESR signal with respect to N-Cs₃Sb₂Br₉, suggesting a higher concentration of Br vacancies in H-Cs₃Sb₂Br₉ than N-Cs₃Sb₂Br₉. This can be verified by the X-ray photoelectron spectrum (XPS) measurements. As shown in Fig. 3e and Fig. S4, the Br 3d and Sb 3d XPS peak of H-Cs₃Sb₂Br₉ exhibited an appreciable shift to the high-energy region (~ 0.23 eV) and low-energy region (~ 0.20 eV) in comparison with that of N-Cs₃Sb₂Br₉, respectively, which proved that H-Cs₃Sb₂Br₉ really has a higher concentration of Br vacancies induced by the absence of surface ligand [41]. In addition, an additional shoulder peak near 532.00 eV can be recognized and attributed to adsorbed oxygen species XPS signal (Fig. S4) at the defect site, with a higher ratio of adsorbed oxygen species XPS signal for H-Cs₃Sb₂Br₉ (38%) than that of N-Cs₃Sb₂Br₉ (13%), also indicating the higher concentration of Br vacancies for H-Cs₃Sb₂Br₉. Furthermore, we also obtained the atom percentage by analyzing EDS elemental peaks of TEM, where the Sb/Br ratios in H-Cs₃Sb₂Br₉ and N-Cs₃Sb₂Br₉ can be determined to be 1/4.01 and 1/4.39 (Fig. S5 and Table S1), respectively, suggesting H-Cs₃Sb₂Br₉ has a high concentration of Br vacancies compared with N-Cs₃Sb₂Br₉. Generally, more anion vacancies contribute to CO₂ adsorption and thus benefit photocatalytic CO₂ reduction [42,43]. This was verified by CO₂ sorption tests (Fig. 3f), in which H-Cs₃Sb₂Br₉ with more abundant Br vacancies exhibited higher CO₂ uptake than N-Cs₃Sb₂Br₉.

To further reveal the role of Br vacancy in affecting the electronic structure of H-Cs₃Sb₂Br₉, the density of state (DOS) and partial density of state (PDOS) were investigated using the Perdue–Burke–Ernzerhof (PBE) of the Generalized Gradient Approximation (GGA) function. As shown in Fig. 3g and h, the valence band maximum (VBM) of Cs₃Sb₂Br₉ was contributed by a filled Br 4p state, and the conduction band minimum (CBM) was mainly composed of empty Sb 5p states, which indicated that the active sites of photocatalytic reduction and oxidation reaction should be the Sb site and Br site, respectively. The generation of Br vacancy could break the rigid octahedron of SbBr₆³⁻, and the unsaturated Sb would be fully exposed for CO₂ adsorption and activation. According to the in-situ irradiated-XPS (ISI-XPS) spectra, the characteristic peaks of Sb 3d and Br 3d XPS in H-Cs₃Sb₂Br₉ shifted to the lower (~ 0.30 eV) and higher (~ 0.23 eV) energy direction after illumination (Fig. S6), respectively. This further verified that Sb and Br could accumulate photogenerated electrons and holes, respectively, and serve as the catalytic sites for photocatalytic reduction and oxidation. Additionally, with the introduction of Br vacancies, the VB edge of H-Cs₃Sb₂Br₉ moves towards low energy which is consistent with the results of UPS spectra (Fig. 3g, h, and Fig. S7). Besides, a shallow acceptor level defect state is formed near the conduction band in the electronic structure of H-Cs₃Sb₂Br₉. The acceptor-like defects originating from Br vacancies could serve as trapping centers to capture photogenerated electrons, and boost the charge separation [44]. As depicted in Fig. 3i, the Sb site near Br vacancy possessed a higher localized charge density, demonstrating that the Sb can act as the active site to promote charge separation and transfer for the photocatalytic reaction [45].

Undoubtedly, the large exposure of catalytic sites, the effective adsorption of reactants, and the charge localization of catalytic sites could effectively improve the electronic communication between photocatalysts and reactants, assisting to improve the catalytic activity.

3.3. Photogenerated carrier dynamics

In general, the photogenerated carrier dynamics properties of photocatalysts could play a pivotal role in determining photocatalytic performance [46–48]. To elucidate the structure-related photogenerated carrier behavior of Cs₃Sb₂Br₉ nanomaterials, we first resorted to the steady-state and transient-state photoluminescence (PL) spectra to monitor the evolution processes of excited carriers in H-Cs₃Sb₂Br₉. As depicted in Fig. S8a, the PL spectra of N-Cs₃Sb₂Br₉ exhibited a strong broad-spectrum emission signal at ca. 520 nm, originating from the intrinsic radiative recombination. While this PL signal in H-Cs₃Sb₂Br₉ was perceptibly weakened concerning that of N-Cs₃Sb₂Br₉, which should result from the effective inhibition of exciton recombination by the abundant surface Br vacancy. With the inhibition of exciton recombination, a large number of free carriers would be energetic to participate in the subsequent redox reaction. The transient PL curves of H-Cs₃Sb₂Br₉ demonstrated an accelerated PL decay in comparison with N-Cs₃Sb₂Br₉ as presented in Fig. S8b. Additionally, the corresponding fitting parameters listed in Table S2 showed that for H-Cs₃Sb₂Br₉, the proportion (A_1) of τ_1 representing charge trapping increased from 34.6% to 77.1%, while the proportion (A_2) of τ_2 representing radiative recombination decreased from 42.0% to 19.8% compared with that of N-Cs₃Sb₂Br₉. These results indicate the effective charge extraction by the abundant Br vacancy on the surface of H-Cs₃Sb₂Br₉. The carrier dynamics were further explored with transient absorption spectroscopy. As demonstrated in nanosecond transient absorption (ns-TA) spectra (Fig. 4a and b), obvious negative signals near 435 nm can be observed upon the excitation of 410 nm laser, which can be attributed to the ground-state bleaching (GSB) signals of Cs₃Sb₂Br₉. The bleach signals mean that the state fillings occurred at which the electrons were on the CB of H-Cs₃Sb₂Br₉ and N-Cs₃Sb₂Br₉, respectively. Compared with N-Cs₃Sb₂Br₉, the annihilation of excited states in H-Cs₃Sb₂Br₉ takes longer. Meanwhile, the kinetic recovery traces at GSB peaks were monitored to evaluate the deactivation process of the photogenerated excitons in the H-Cs₃Sb₂Br₉ and N-Cs₃Sb₂Br₉ materials (Fig. 4c). For H-Cs₃Sb₂Br₉, a prolonged delayed GSB recovery process can be achieved, with an averaged lifetime of 9.11 ± 0.16 ns compared with that of N-Cs₃Sb₂Br₉ (1.63 ± 0.04 ns) (Table S3). This phenomenon should be attributed to the shallow trap levels generated by Br vacancies, which can capture photogenerated electrons, suppress charge recombination, and then meliorate charge separation of H-Cs₃Sb₂Br₉. Thus the carriers in H-Cs₃Sb₂Br₉ would have a higher probability to transfer to the surface to participate in the redox reaction [49].

The favorable charge separation benefitting from the Br vacancies can be further validated by measuring the open-circuit photovoltage decay (OCVD) curves of H-Cs₃Sb₂Br₉ and N-Cs₃Sb₂Br₉ (Fig. S9). Thanks to excellent space charge separation induced by Br vacancy, H-Cs₃Sb₂Br₉ exhibited higher open-circuit photovoltage over N-Cs₃Sb₂Br₉. The corresponding photoinduced non-equilibrium carrier lifetime (τ_n) plots can be obtained according to the equation $\tau_n = -k_B T/e(dV_oc/dt)^{-1}$, where k_B , T , and e denote Boltzmann constant, temperature, and electron charge, respectively [50]. As presented in Fig. 4d, H-Cs₃Sb₂Br₉ displays a prolonged electron lifetime in contrast to N-Cs₃Sb₂Br₉, indicating that the photogenerated electrons in H-Cs₃Sb₂Br₉ have more opportunities to migrate to the catalytic sites to participate in the catalytic reaction. In addition, the non-equilibrium carrier concentrations of H-Cs₃Sb₂Br₉ and N-Cs₃Sb₂Br₉ can be derived from the corresponding Mott–Schottky curves according to the Mott–Schottky equation (Table S4, see the Supporting Information). As illustrated in Fig. 4e, H-Cs₃Sb₂Br₉ exhibited a decreased curve slope compared with N-Cs₃Sb₂Br₉, implying the higher non-equilibrium carrier concentration

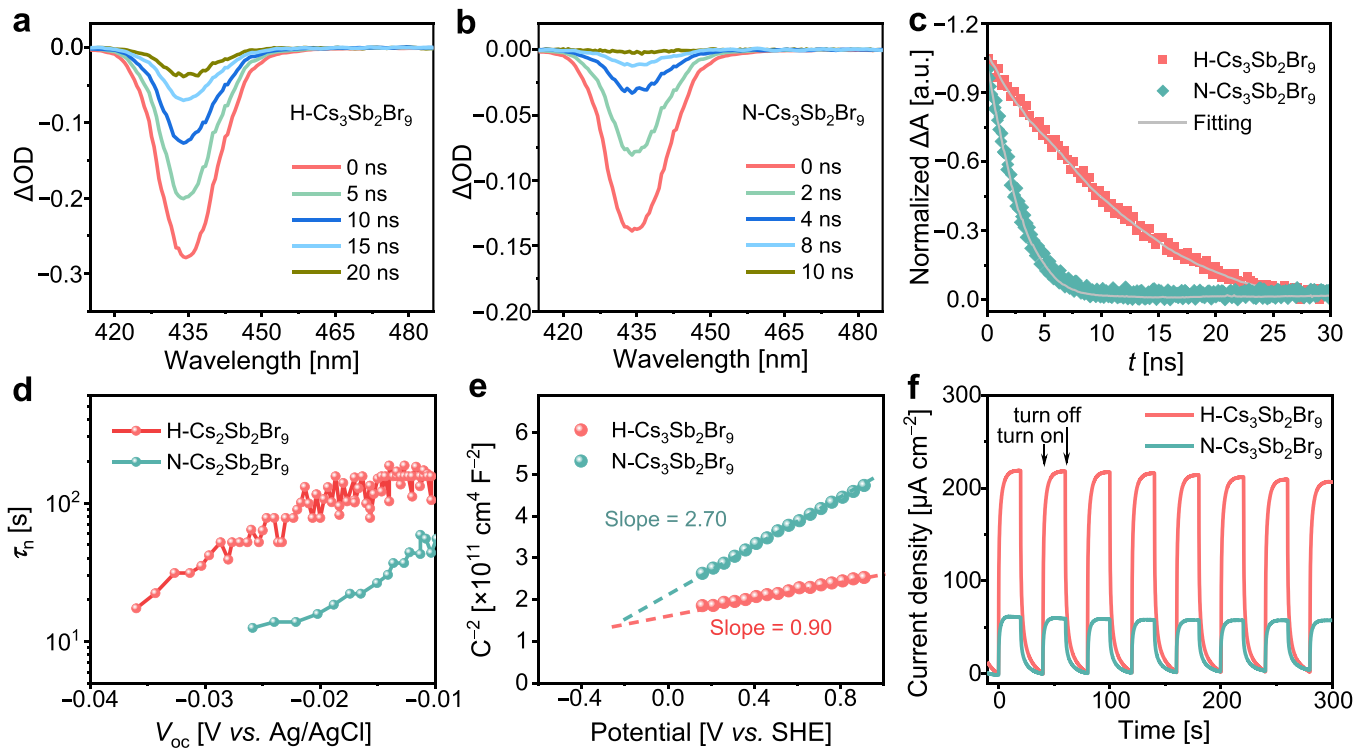


Fig. 4. Nanosecond transient absorption (ns-TA) spectra at indicated delay time after 410 nm optical excitation of (a) H-Cs₃Sb₂Br₉ and (b) N-Cs₃Sb₂Br₉. (c) ns-TA kinetic plots of H-Cs₃Sb₂Br₉ and N-Cs₃Sb₂Br₉ monitored at respective GSB peaks. (d) The non-equilibrium carrier lifetime plots of H-Cs₃Sb₂Br₉ and N-Cs₃Sb₂Br₉ converted from the corresponding OCVD decay curves. (e) The Mott–Schottky plots for H-Cs₃Sb₂Br₉ and N-Cs₃Sb₂Br₉ under light irradiation. (f) $I-t$ curves of H-Cs₃Sb₂Br₉ and N-Cs₃Sb₂Br₉.

in H-Cs₃Sb₂Br₉. The specific carrier concentration values of H-Cs₃Sb₂Br₉ and N-Cs₃Sb₂Br₉ could be calculated at 6.82×10^{19} and 2.27×10^{19} cm⁻³, respectively (Table S4). Moreover, transient photocurrent responses ($I-t$) were performed to throw light on the transfer and separation capability of the photogenerated carriers in H-Cs₃Sb₂Br₉. As shown in Fig. 4f, it is clear to see that H-Cs₃Sb₂Br₉ displays distinctly enhanced photocurrent intensity compared to N-Cs₃Sb₂Br₉, implying a more efficient photogenerated carrier separation of H-Cs₃Sb₂Br₉ over N-Cs₃Sb₂Br₉. The more non-equilibrium carriers that participate in the redox reactions should be in favor of the enhancement of photocatalytic activity [51,52].

3.4. Interfacial interaction and charge transfer

Benefiting from the larger specific surface area, excellent light harvesting, abundant surface sites, and remarkable excited carrier properties, H-Cs₃Sb₂Br₉ should be an ideal photocatalyst, and can be suitable for combining with cocatalysts to construct efficient photocatalytic systems. Considering the potential matching of H-Cs₃Sb₂Br₉ and co-catalysts (Fig. S10), we selected a dinuclear cobalt molecular catalyst (Co₂L) as the co-catalyst [34]. As the zeta potential of Co₂L was reversed with that of H-Cs₃Sb₂Br₉ in the same condition (Fig. S11), the combination of Co₂L with H-Cs₃Sb₂Br₉ (Co₂L-H-Cs₃Sb₂Br₉) can be driven by electrostatic interactions. As a reference, the Co₂L-N-Cs₃Sb₂Br₉ composite was also prepared and evaluated under identical conditions. The TEM and corresponding EDS mapping images (Figs. S12 and S13) verified the homogeneous distribution of Co₂L on the surface of H-Cs₃Sb₂Br₉ and N-Cs₃Sb₂Br₉. Furthermore, the XRD patterns of the composite photocatalysts demonstrated that there was no structure change for Cs₃Sb₂Br₉ after compositing with Co₂L (Fig. S14). It is worth noting that a significant displacement occurred for element binding energy in XPS spectra of Co₂L-H-Cs₃Sb₂Br₉ with respect to individual H-Cs₃Sb₂Br₉ and Co₂L. In contrast, a tiny displacement for element

binding energy of Co₂L-N-Cs₃Sb₂Br₉ with respect to individual N-Cs₃Sb₂Br₉ and Co₂L (Fig. 5). These results indicate a much stronger electronic coupling between H-Cs₃Sb₂Br₉ and Co₂L, which endows the interface between Co₂L and H-Cs₃Sb₂Br₉ with excellent electronic communication capability. In addition, according to the ISI-XPS spectra, the characteristic peaks of Co 2p XPS in Co₂L-H-Cs₃Sb₂Br₉ shifted to the lower binding energy under illumination (Fig. S15), indicating that Co can accept excited electrons and act as the activity site for the CO₂ photoreduction.

The charge transfer characteristics of Co₂L-H-Cs₃Sb₂Br₉ and Co₂L-N-Cs₃Sb₂Br₉ were further evaluated by PL spectra. As shown in Fig. S16, the PL intensity of H-Cs₃Sb₂Br₉ quenched much greater (88%) compared with that of N-Cs₃Sb₂Br₉ (15%) after combining with Co₂L, indicating highly effective interface charge transfer from H-Cs₃Sb₂Br₉ to Co₂L. Furthermore, more obvious transient PL decay was observed for Co₂L-H-Cs₃Sb₂Br₉ than Co₂L-N-Cs₃Sb₂Br₉, which firmly confirmed the effect of the ligand-free H-Cs₃Sb₂Br₉ on boosting electronic communication efficiency (Fig. S17 and Table S5). The efficient electronic communication between H-Cs₃Sb₂Br₉ and Co₂L would generate more photogenerated charges, as further evidenced by the Mott–Schottky plots and photocurrent curves (Figs. S18 and S19, and Table S6), and accordingly, enhance the electronic conduction capability (Fig. S20 and Table S7). In all, these above results demonstrate that the ligand-free H-Cs₃Sb₂Br₉ can effectively accelerate the interfacial electronic transfer between H-Cs₃Sb₂Br₉ and Co₂L, which should be beneficial to the enhancement of photocatalytic activity.

3.5. Photocatalytic activity

The photocatalytic CO₂ reduction experiments of Co₂L-H-Cs₃Sb₂Br₉ and referenced photocatalysts were performed in a gas–solid reaction system filled with CO₂ as well as H₂O and CH₃OH vapor (Fig. S21, the details were described in the Methods section). As depicted in Fig. S22,

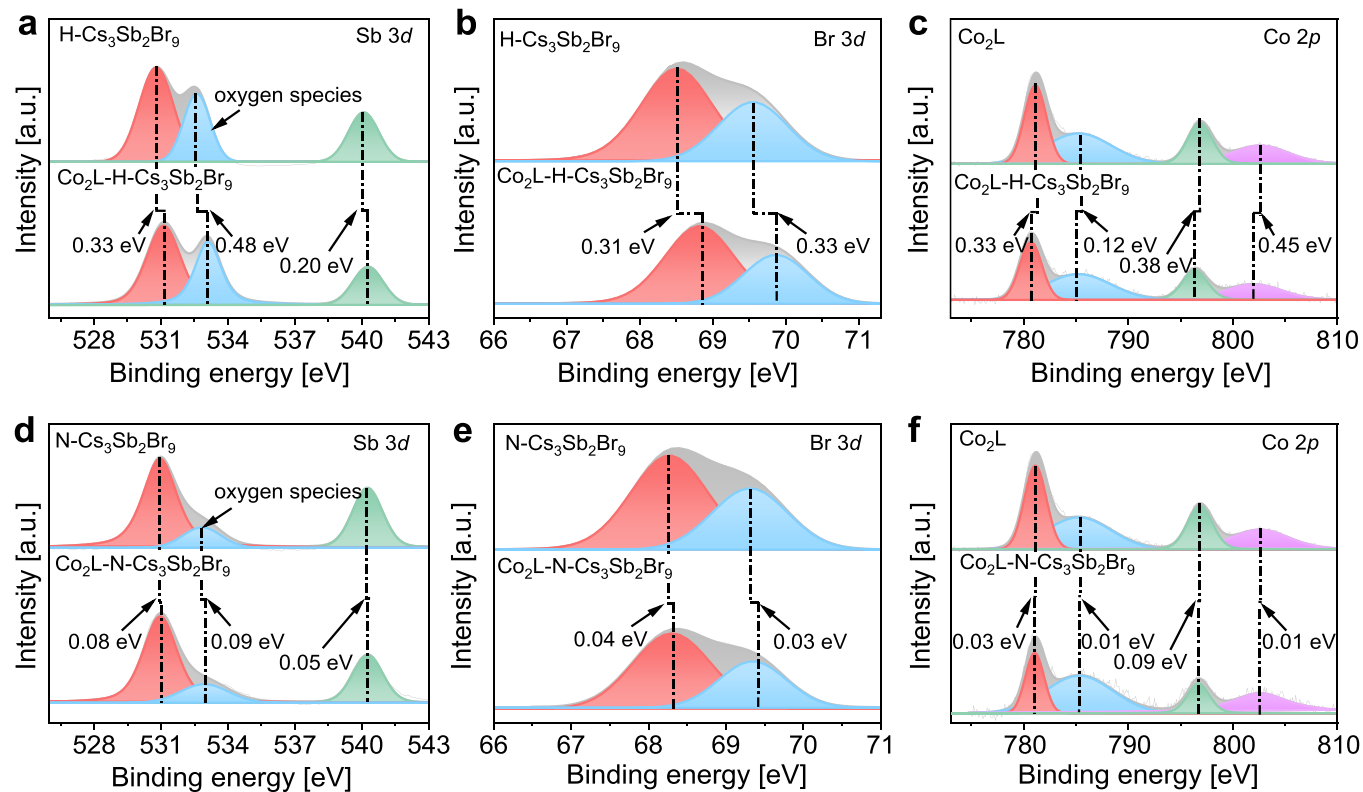


Fig. 5. High-resolution XPS of H-Cs₃Sb₂Br₉, N-Cs₃Sb₂Br₉, Co₂L, Co₂L-H-Cs₃Sb₂Br₉, and Co₂L-N-Cs₃Sb₂Br₉: (a, d) Sb 3d, (b, e) Br 3d, and (c, f) Co 2p.

H-Cs₃Sb₂Br₉ can efficiently reduce CO₂ to CO, with almost no H₂ and hydrocarbon products detected under visible light irradiation. The time-dependent CO production curves (Fig. 6a) of H-Cs₃Sb₂Br₉ demonstrated the significantly superior photocatalytic CO₂ reduction activity to N-Cs₃Sb₂Br₉. The CO production of H-Cs₃Sb₂Br₉ reached up to 5059.7

± 169.6 $\mu\text{mol g}^{-1}$ after 8 h of photocatalytic reaction, almost 13 folds over that of N-Cs₃Sb₂Br₉ (400.0 ± 35.2 $\mu\text{mol g}^{-1}$). The activity improvement should be attributed to the fact discussed above, that is, ligand-free H-Cs₃Sb₂Br₉ hollow nanospheres possess enhanced light-

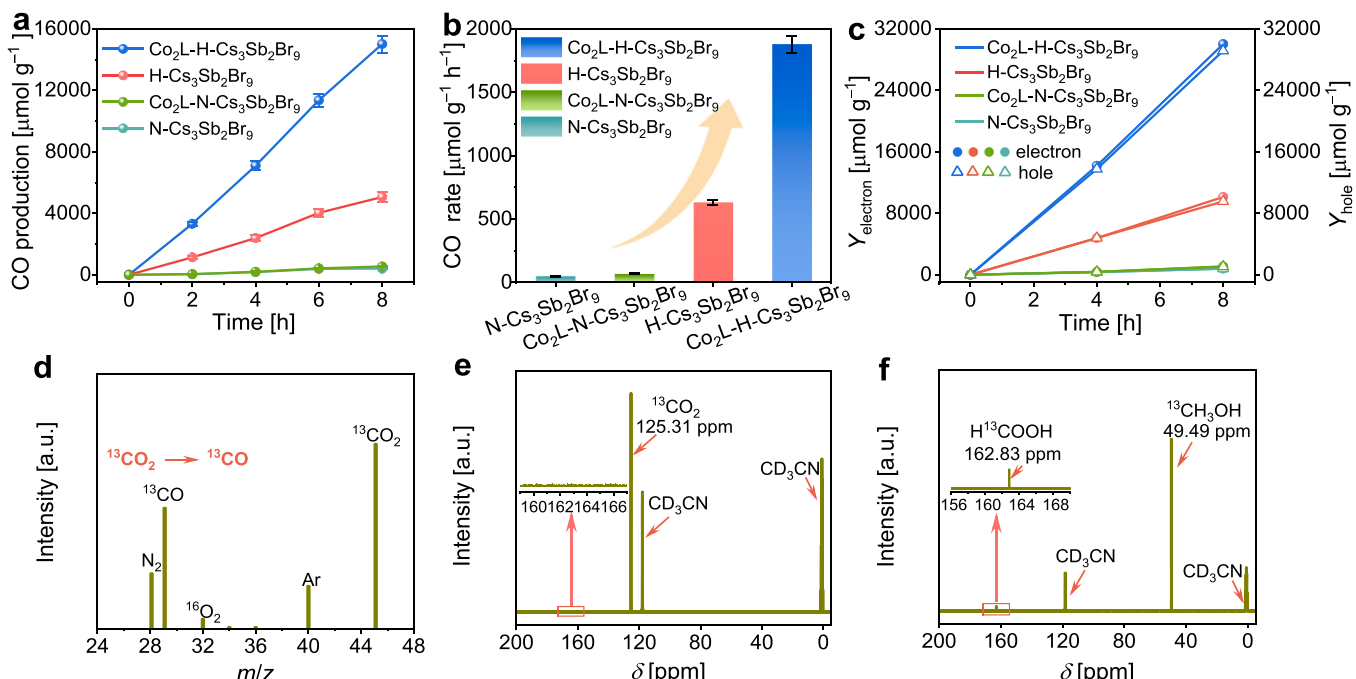


Fig. 6. The CO production (Y_{CO}) (a), CO generation rate (b) as well as electron ($\text{Y}_{\text{electron}}$) and hole (Y_{hole}) consumption (c) of photocatalytic CO₂ reduction coupled with CH₃OH oxidation ($\text{Y}_{\text{electron}} = 2 \times \text{Y}_{\text{CO}}$ and $\text{Y}_{\text{hole}} = 4 \times \text{Y}_{\text{HCOOH}}$). (d) The MS spectra of the gas products generated from the photocatalytic ¹³CO₂ reduction reaction. The ¹³C NMR spectra for the products obtained from the reaction with ¹³CO₂/CH₃OH (e) and CO₂/¹³CH₃OH (f) as feedstocks by using Co₂L-H-Cs₃Sb₂Br₉ as the photocatalyst.

harvesting, more exposed catalytic sites, more effective charge separation and transfer, as well as more active surface reactivity over N-Cs₃Sb₂Br₉ nanocrystals. For comparison, we also prepared N-Cs₃Sb₂Br₉-220 with a size of 220 nm, with similar light absorption to N-Cs₃Sb₂Br₉ (Fig. S23a and b). N-Cs₃Sb₂Br₉-220 obtained $75.0 \pm 3.2 \mu\text{mol g}^{-1}$ of CO production, much lower than that of H-Cs₃Sb₂Br₉ and N-Cs₃Sb₂Br₉ (Fig. S23c), which can be ascribed to the decrease in catalytic sites due to the decrease of specific surface area. In addition, we optimized the synthesis process of Br-rich vacancy H-Cs₃Sb₂Br₉ by controlling the ratio between CsBr and SbBr₃ (3/1.5, 3/2, and 3/2.5) in the precursor. Three types of H-Cs₃Sb₂Br₉ with low, middle, and high concentrations of Br vacancies (note as H-Cs₃Sb₂Br₉-L, H-Cs₃Sb₂Br₉, and H-Cs₃Sb₂Br₉-H) can be obtained (Fig. S24a). The photocatalytic results show that the concentration of Br vacancies on H-Cs₃Sb₂Br₉ has an important influence on photocatalytic performance. Increasing the concentration of Br vacancy brings forth a volcanic tendency of R_{electron} (Fig. S24b), which should be due to the increase of active sites and the decrease of carrier mobility.

Encouraged by the excellent photocatalytic activity of H-Cs₃Sb₂Br₉, the performance of Co₂L-H-Cs₃Sb₂Br₉ was further investigated. As shown in Fig. 6a and b, a remarkable improvement was achieved with Co₂L-H-Cs₃Sb₂Br₉ for photocatalytic CO₂ reduction with respect to Co₂L-N-Cs₃Sb₂Br₉. Specifically, Co₂L-H-Cs₃Sb₂Br₉ exhibited an unprecedented CO production of $15,010.4 \pm 550.4 \mu\text{mol g}^{-1}$ (selectivity nearly to 100%) in 8 h, 28 folds than that of Co₂L-N-Cs₃Sb₂Br₉ ($544.0 \pm 41.6 \mu\text{mol g}^{-1}$). The corresponding CO generation rate of Co₂L-H-Cs₃Sb₂Br₉ is $1876.3 \pm 68.8 \mu\text{mol g}^{-1} \text{ h}^{-1}$, which is over 38, 28, and 3 folds than those of pure N-Cs₃Sb₂Br₉ ($50.0 \pm 4.4 \mu\text{mol g}^{-1} \text{ h}^{-1}$), Co₂L-N-Cs₃Sb₂Br₉ ($68.1 \pm 5.2 \mu\text{mol g}^{-1} \text{ h}^{-1}$), and pure H-Cs₃Sb₂Br₉ ($632.5 \pm 31.2 \mu\text{mol g}^{-1} \text{ h}^{-1}$), respectively. Moreover, the photocatalytic activity of Co₂L-H-Cs₃Sb₂Br₉ is also the highest among reported MHPs-based photocatalysts; The electron consumption rate of Co₂L-H-Cs₃Sb₂Br₉ ($3752.6 \mu\text{mol g}^{-1} \text{ h}^{-1}$) for CO₂ photoreduction is much higher than those of reported MHPs-based photocatalysts (Table S8). The corresponding turnover frequency (TOF) based on the Co₂L can be calculated to be 157.82 h^{-1} , and the apparent quantum yield (AQY) reaches 2.65% at 400 nm. Obviously, the excellent photocatalytic activity of Co₂L-H-Cs₃Sb₂Br₉ can be ascribed to unique semiconductor features, that is, strong light adsorption, fast charge separation and transfer, as well as high surface reactivity, which is closely related to the ligand-free hollow nano-spherical structure.

We have also examined the oxidation products during the photocatalytic CO₂ reduction with Co₂L-H-Cs₃Sb₂Br₉ by ion chromatography. It was found that there were no liquid products detected in the absence of CH₃OH, while formic acid could be distinctly detected in the presence of CH₃OH (Fig. S25). These observations implied that the detected formic acid may come from the oxidation of CH₃OH by the holes of Co₂L-H-Cs₃Sb₂Br₉ generated from the CO₂ reduction. As shown in Fig. S26, the generation rate of formic acid for H-Cs₃Sb₂Br₉ is $298.1 \pm 12.2 \mu\text{mol g}^{-1} \text{ h}^{-1}$, which is 12 folds higher than that of N-Cs₃Sb₂Br₉. It is more exciting that the photocatalytic activity of Co₂L-H-Cs₃Sb₂Br₉ improved to an unprecedented level, with the yield of formic acid reaching as high as $910.6 \pm 33.8 \mu\text{mol g}^{-1} \text{ h}^{-1}$, much higher than that of Co₂L-N-Cs₃Sb₂Br₉ ($33.1 \pm 3.3 \mu\text{mol g}^{-1} \text{ h}^{-1}$). The excellent photocatalytic activity of Co₂L-H-Cs₃Sb₂Br₉ should also be attributed to its ligand-free hollow nano-spherical structure, which enables close interfacial contact between H-Cs₃Sb₂Br₉ and Co₂L, and thus fast electronic transfer from H-Cs₃Sb₂Br₉ to Co₂L. The remaining large number of holes then fast oxidize CH₃OH to formic acid. Based on the above discussion, the whole photocatalytic reactions containing CO₂ reduction and CH₃OH oxidation by Co₂L-H-Cs₃Sb₂Br₉ can be described as $2\text{CO}_2 + \text{CH}_3\text{OH} \rightarrow 2\text{CO} + \text{HCOOH} + \text{H}_2\text{O}$. According to the formula of $Y_{\text{electron}} = 2 \times Y_{\text{CO}}$ and $Y_{\text{hole}} = 4 \times Y_{\text{HCOOH}}$, the consumed amount of electrons for the conversion of CO₂ to CO and the consumed amount of holes for CH₃OH oxidation to formic acid were calculated. The results in Fig. 6c clearly show that the amount of consumed electrons is equal to that of holes, demonstrating an effective utilization of the photogenerated electrons and holes. In addition, after

the photocatalytic reaction, it can be seen that no obvious change occurred in XRD patterns (Fig. S27), XPS (Fig. S28), SEM and TEM images (Fig. S29) for Co₂L-H-Cs₃Sb₂Br₉, indicating its good stability in the photocatalytic reaction.

To explore the origin of CO and HCOOH during the photocatalytic CO₂ reduction and CH₃OH oxidation, a series of controlled photocatalytic experiments were performed with Co₂L-H-Cs₃Sb₂Br₉ as a photocatalyst (Fig. S30). The results of GC show that there is no gas product detected under the conditions of no Co₂L-H-Cs₃Sb₂Br₉, no light, or no CO₂, implying that the CO was produced over the light-driven reduction of CO₂ by Co₂L-H-Cs₃Sb₂Br₉. This was further confirmed by the ¹³CO₂ isotope labeling experiment, where an obvious ¹³CO (*m/z* = 29) signal can be detected during the photocatalytic CO₂ reduction by Co₂L-H-Cs₃Sb₂Br₉ when using ¹³CO₂ instead of ¹²CO₂ (Fig. 6d). In addition, the ¹³C NMR spectra of the liquid products of the photocatalytic CO₂ reduction reaction with Co₂L-H-Cs₃Sb₂Br₉ by using CH₃OH and ¹³CO₂ as well as ¹³CH₃OH and CO₂ as feedstocks were measured, respectively. As presented in Fig. 6e, besides the characteristic peaks identified for the solvent and ¹³CO₂ (117.91 ppm and 0.90 ppm for CD₃CN, 125.36 ppm for ¹³CO₂), no peak can be detected in the ¹³C NMR spectrum of the photocatalytic reaction system with ¹³CO₂ and CH₃OH as feedstocks, ruling out the occurrence of CO₂ reduction to formic acid. On the contrary, when using CO₂ and ¹³CH₃OH as the feedstocks, a clear characteristic peak at 163.57 ppm corresponding to the H¹³COO⁻ can be identified (Fig. 6f) in the ¹³C NMR spectrum, confirming that the liquid product formic acid indeed originated from the CH₃OH oxidation.

3.6. The mechanisms of CO₂ photoreduction coupled with CH₃OH oxidation

Based on the above results, the mechanisms of CO₂ photoreduction coupled with CH₃OH oxidation could be proposed. For H-Cs₃Sb₂Br₉, the Sb and Br would be simultaneously served as the reduction and oxidation sites, respectively (Fig. 7a). Under illumination, H-Cs₃Sb₂Br₉ was excited by light to generate electrons and holes. Thanks to the excellent charge separation of H-Cs₃Sb₂Br₉, photogenerated electrons were accumulated at the Sb site, and to reduce the adsorbed CO₂ to CO through the proton-coupled electron transfer (PCET) process. As shown in the free-energy pathways (Fig. 7b), the following steps were mainly undergone during photocatalytic CO₂ reduction with H-Cs₃Sb₂Br₉ (CO₂ + 2e⁻ + 2H⁺ → CO + H₂O) [53]: 1) The adsorbed CO₂ on the Sb site was first activated to form CO₂^{*} species. 2) With the protonation of CO₂^{*} species, COOH^{*} species can be generated. 3) The CO^{*} can be obtained with the successively protonating and dehydrating of COOH^{*} species. 4) The obtained CO^{*} was desorbed from the H-Cs₃Sb₂Br₉ to generate CO product. It should be mentioned that a competitive reaction of CO^{*} desorption, that is, further protonation of the obtained CO^{*} to form CHO^{*} may occur (Fig. 7b). However, this step was endothermic, and the free energy change (ΔG) is much higher than that for CO^{*} desorption. This explained that H-Cs₃Sb₂Br₉ possesses high selectivity to CO (nearly 100%) in the photocatalytic CO₂ reduction reaction. For the Co₂L-H-Cs₃Sb₂Br₉, the Co^{II} within Co₂L would be acted as the reduction sites. Benefiting from excellent electronic communication between H-Cs₃Sb₂Br₉ and Co₂L, photogenerated electrons transferred from H-Cs₃Sb₂Br₉ to Co₂L rapidly, and also reduce the CO₂ to CO through PCET processes (Fig. 7c). Specifically, the adsorbed CO₂ formed a carbonate-bridged complex with Co₂L, and then underwent a PCET process to generate *CO₃H⁻. The *CO₃H⁻ was protonated and then dehydrated to form *CO₂⁻, and subsequently went through a PCET process again to generate *COOH. Finally, the CO can be obtained following the cleavage of the C–OH bond and the release of *CO [34].

To explore the CH₃OH oxidation process, in-situ Raman spectroscopy was measured to monitor the evolution of surface species on photocatalysts. As shown in Fig. 7d, due to the adsorption of CH₃OH

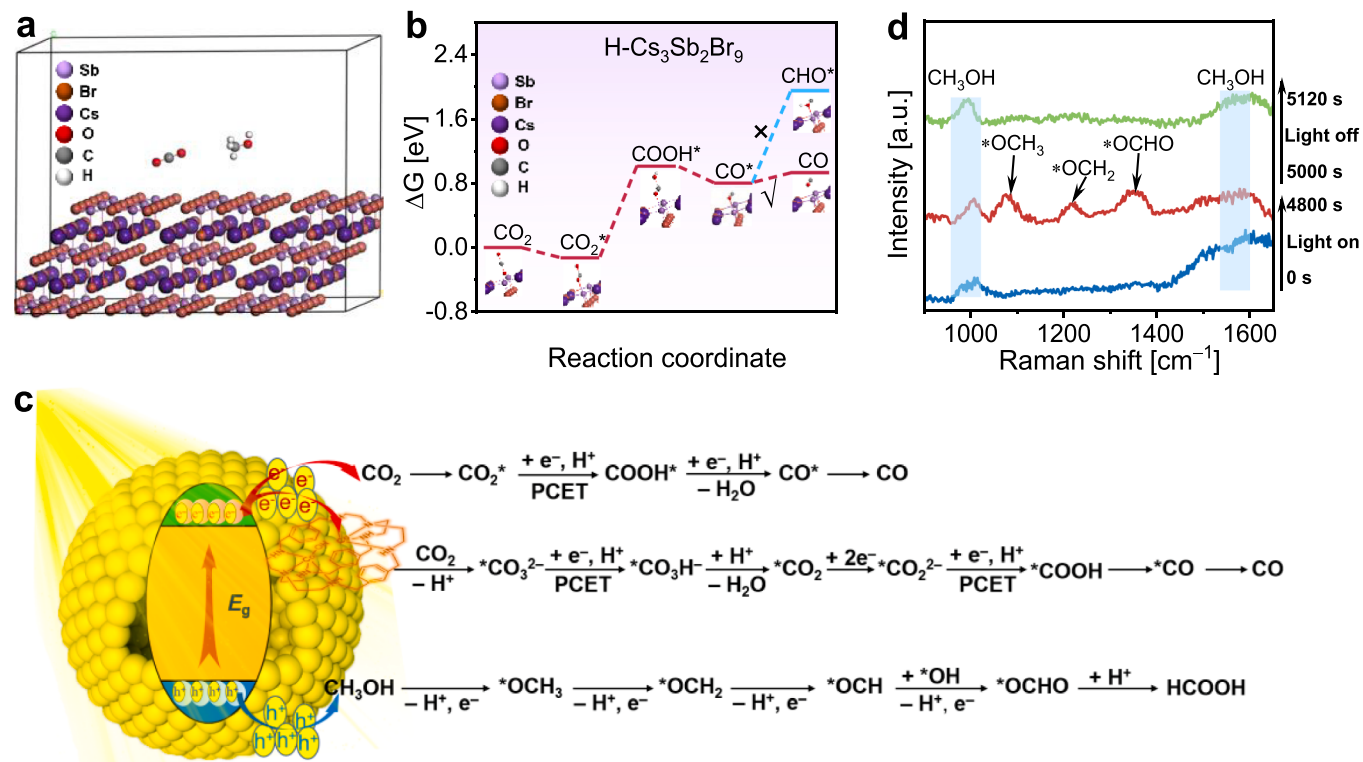


Fig. 7. (a) The structural model of H-Cs₃Sb₂Br₉ exposed unsaturated Sb for photocatalytic CO₂ reduction. (b) Free-energy pathways of H-Cs₃Sb₂Br₉ with Sb as activity sites for photocatalytic CO₂ reduction. (c) The reaction mechanism of photocatalytic CO₂ reduction coupled with CH₃OH oxidation by Co₂L-H-Cs₃Sb₂Br₉. (d) In-situ Raman spectroscopy to monitor the intermediates of photocatalytic CH₃OH oxidation (Conditions: oxygen is used as the electron capture agent during the measurement).

molecules, two absorption peaks appeared at 1014 and 1540 cm⁻¹ before illumination [54]. While as the continuous illumination went on, another peak at 1060 cm⁻¹ was generated and identified as *OCH₃, which was mainly caused by the dehydrogenation of -OH in CH₃OH molecules [55]. Meanwhile, the peaks at 1214 and 1353 cm⁻¹ were identified as the *OCH₂ and *OCHO, respectively. Based on the above results, the reaction process of photocatalytic CH₃OH oxidation to formic acid could be described in Fig. 7c. Specifically, the photogenerated holes were accumulated at the Br site, and oxidized the CH₃OH to HCOOH by a continuous multi-step deprotonation and hydroxylation process [56,57]. First, the -OH group of CH₃OH underwent a dehydrogenation step to generate *OCH₃, and then followed by two consecutive C-H bond breaking, generating two key intermediates of *OCH₂ and *OCH. The obtained *OCH would bond with an O atom from OH group to generate *OCHO. Finally, the *OCHO followed by desorbing and forming the liquid product HCOOH.

4. Conclusions

In summary, a lead-free Cs₃Sb₂Br₉ hollow nanosphere was successfully constructed by a facile antisolvent-assistant method. The obtained lead-free Cs₃Sb₂Br₉ hollow nanosphere shows high photocatalytic activity for CO₂ reduction coupled with CH₃OH oxidation. Under visible-light irradiation, a record electron consumption rate of 3752.6 ± 137.6 μmol g⁻¹ h⁻¹ can be achieved for CO₂ photoreduction, while simultaneously generating nearly stoichiometric amounts of value-added formic acid. The excellent photocatalytic activity can be attributed to the ligand-free hollow structure of H-Cs₃Sb₂Br₉. These structural features endow H-Cs₃Sb₂Br₉ with enhanced light-absorption ability, effective charge separation and transfer, as well as high surface reactivity. This work provides an efficacious scheme for the development of efficient halide perovskite-based photocatalysts for CO₂ reduction.

CRediT authorship contribution statement

Yan-Fei Mu: Methodology, Investigation, Writing – original draft. **Jin-Shuang Zhao:** Investigation. **Li-Yuan Wu:** Investigation. **Ke-Ying Tao:** Investigation. **Zhao-Lei Liu:** Investigation. **Fu-Quan Bai:** Methodology, Investigation. **Di-Chang Zhong:** Conceptualization, Writing – review & editing, Funding acquisition, Resources, Supervision. **Min Zhang:** Conceptualization, Methodology, Writing – review & editing, Funding acquisition, Resources, Supervision. **Tong-Bu Liao:** Conceptualization, Writing – review & editing, Funding acquisition, Resources, Supervision.

Declaration of Competing Interest

The authors declare that they have no known competing financial interests or personal relationships that could have appeared to influence the work reported in this paper.

Data Availability

Data will be made available on request.

Acknowledgments

This work was financially supported by the National Key R&D Program of China (2022YFA1502902), NSFC (21931007, 22271218, 22071182, U21A20286), the Natural Science Foundation of Tianjin City (17JCJQJC43800), the Jiangsu Funding Program for Excellent Postdoctoral Talent, the 111 Project of China (D17003) and Tianjin Research Innovation Project for Postgraduate Students (2021YJSB253).

Appendix A. Supporting information

Supplementary data associated with this article can be found in the online version at doi:10.1016/j.apcatb.2023.123024.

References

- 1 A. Wagner, C.D. Sahm, E. Reisner, Towards molecular understanding of local chemical environment effects in electro- and photocatalytic CO_2 reduction, *Nat. Catal.* 3 (2020) 775–786.
- 2 S. Navarro-Jaén, M. Virginie, J. Bonin, M. Robert, R. Wojcieszak, A.Y. Khodakov, Highlights and challenges in the selective reduction of carbon dioxide to methanol, *Nat. Rev. Chem.* 5 (2021) 564.
- 3 J.Y.Y. Loh, N.P. Kherani, G.A. Ozin, Persistent CO_2 photocatalysis for solar fuels in the dark, *Nat. Sustain.* 4 (2021) 466–473.
- 4 M. Ding, R.W. Flraig, H.-L. Jiang, O.M. Yaghi, Carbon capture and conversion using metal-organic frameworks and MOF-based materials, *Chem. Soc. Rev.* 48 (2019) 2783–2828.
- 5 F. Xu, K. Meng, B. Cheng, S. Wang, J. Xu, J. Yu, Unique S-scheme heterojunctions in self-assembled $\text{TiO}_2/\text{CsPbBr}_3$ hybrids for CO_2 photoreduction, *Nat. Commun.* 11 (2020) 4613.
- 6 Y. Jiang, J.-F. Liao, H.-Y. Chen, H.-H. Zhang, J.-Y. Li, X.-D. Wang, D.-B. Kuang, All-solid-state Z-scheme $\alpha\text{-Fe}_2\text{O}_3$ /Amine-RGO/CsPbBr₃ hybrids for visible-light-driven photocatalytic CO_2 reduction, *Chem.* 6 (2020) 766–780.
- 7 Y. Li, S. Wang, X.-S. Wang, Y. He, Q. Wang, Y. Li, M. Li, G. Yang, J. Yi, H. Lin, D. Huang, L. Li, H. Chen, J. Ye, Facile top-down strategy for direct metal atomization and coordination achieving a high turnover number in CO_2 photoreduction, *J. Am. Chem. Soc.* 142 (2020) 19259–19267.
- 8 D. Long, J. Liu, H. Chen, P. Liu, K. Zheng, Y. Zeng, X. Chen, S. Li, M. Lu, Electronegativity diversity induced localized built-in electric field in a single phased $\text{MoS}_x\text{Se}_y\text{N}_z$ for selectivity-enhanced visible photocatalytic CO_2 reduction, *Appl. Catal. B-Environ.* 330 (2023), 122625.
- 9 M. Li, L. Shen, M.-Q. Yang, Cobalt-based cocatalysts for photocatalytic CO_2 reduction, *Trans. Tianjin Univ.* 28 (2022) 506–532.
- 10 R. Chen, Z. Ren, Y. Liang, G. Zhang, T. Dittrich, R. Liu, Y. Liu, Y. Zhao, S. Pang, H. An, C. Ni, P. Zhou, K. Han, F. Fan, C. Li, Spatiotemporal imaging of charge transfer in photocatalyst particles, *Nature* 610 (2022) 296–301.
- 11 Y. Miao, Y. Zhao, S. Zhang, R. Shi, T. Zhang, Strain engineering: a boosting strategy for photocatalysis, *Adv. Mater.* 34 (2022) 2200868.
- 12 Z. Xing, J. Hu, M. Ma, H. Lin, Y. An, Z. Liu, Y. Zhang, J. Li, S. Yang, From one to two: in situ construction of an ultrathin 2D–2D closely bonded heterojunction from a single-phase monolayer nanosheet, *J. Am. Chem. Soc.* 141 (2019) 19715–19727.
- 13 Q. Lei, H. Yuan, J. Du, M. Ming, S. Yang, Y. Chen, J. Lei, Z. Han, Photocatalytic CO_2 reduction with aminoanthraquinone organic dyes, *Nat. Commun.* 14 (2023) 1087.
- 14 H. Zhang, J. Nai, L. Yu, X.W. Lou, Metal-organic-framework-based materials as platforms for renewable energy and environmental applications, *Joule* 1 (2017) 77–107.
- 15 M. Zhang, M. Lu, Z.-L. Lang, J. Liu, M. Liu, J.-N. Chang, L.-Y. Li, L.-J. Shang, M. Wang, S.-L. Li, Y.-Q. Lan, Semiconductor/covalent-organic-framework Z-scheme heterojunctions for artificial photosynthesis, *Angew. Chem. Int. Ed.* 59 (2020) 6500–6505.
- 16 Q. Wang, J. Warnan, S. Rodríguez-Jiménez, J.J. Leung, S. Kalathil, V. Andrei, K. Domen, E. Reisner, Molecularly engineered photocatalyst sheet for scalable solar formate production from carbon dioxide and water, *Nat. Energy* 5 (2020) 703–710.
- 17 M. Yang, P. Wang, Y. Li, S. Tang, X. Lin, H. Zhang, Z. Zhu, F. Chen, Graphene aerogel-based $\text{NiAl-LDH}/\text{g-C}_3\text{N}_4$ with ultratight sheet-sheet heterojunction for excellent visible-light photocatalytic activity of CO_2 reduction, *Appl. Catal. B-Environ.* 306 (2022), 121065.
- 18 M.V. Kovalenko, L. Protesescu, M.I. Bodnarchuk, Properties and potential optoelectronic applications of lead halide perovskite nanocrystals, *Science* 358 (2017) 745–750.
- 19 Y. Hassan, J.H. Park, M.L. Crawford, A. Sadhanala, J. Lee, J.C. Sadighian, E. Mosconi, R. Shivanna, E. Radicchi, M. Jeong, C. Yang, H. Choi, S.H. Park, M. H. Song, F. De Angelis, C.Y. Wong, R.H. Friend, B.R. Lee, H.J. Snaith, Ligand-engineered bandgap stability in mixed-halide perovskite LEDs, *Nature* 591 (2021) 72–77.
- 20 X.-K. Liu, W. Xu, S. Bai, Y. Jin, J. Wang, R.H. Friend, F. Gao, Metal halide perovskites for light-emitting diodes, *Nat. Mater.* 20 (2021) 10–21.
- 21 J. Luo, X. Wang, S. Li, J. Liu, Y. Guo, G. Ni, L. Yao, Y. Fu, L. Gao, Q. Dong, C. Zhao, M. Leng, F. Ma, W. Liang, L. Wang, S. Jin, J. Han, L. Zhang, J. Etheridge, J. Wang, Y. Yan, E.H. Sargent, J. Tang, Efficient and stable emission of warm-white light from lead-free halide double perovskites, *Nature* 563 (2018) 541–545.
- 22 B. Yang, J. Chen, S. Yang, F. Hong, L. Sun, P. Han, T. Pullerits, W. Deng, K. Han, Lead-free silver-bismuth halide double perovskite nanocrystals, *Angew. Chem. Int. Ed.* 57 (2018) 5359–5363.
- 23 S. Chen, H. Yin, P. Liu, Y. Wang, H. Zhao, Stabilization and performance enhancement strategies for halide perovskite photocatalysts, *Adv. Mater.* 35 (2023) 2203836.
- 24 E. Danladi, M. Kashif, A. Ichoja, B.B. Aiyaya, Modeling of a Sn-based HTM-free perovskite solar cell using a one-dimensional solar cell capacitance simulator tool, *Trans. Tianjin Univ.* 29 (2023) 62–72.
- 25 J.-Y. Gu, P.-W. Qi, Y. Peng, Progress on the development of inorganic lead-free perovskite solar cells, *Acta Phys. Chim. Sin.* 33 (2017) 1379–1389.
- 26 Z. Xiao, W. Meng, J. Wang, D.B. Mitzi, Y. Yan, Searching for promising new perovskite-based photovoltaic absorbers: the importance of electronic dimensionality, *Mater. Horiz.* 4 (2017) 206–216.
- 27 M.-G. Ju, J. Dai, L. Ma, Y. Zhou, X.-C. Zeng, Zero-dimensional organic–inorganic perovskite variant: transition between molecular and solid crystal, *J. Am. Chem. Soc.* 140 (2018) 10456–10463.
- 28 T. Li, S. Luo, X. Wang, L. Zhang, Alternative lone-pair ns^2 -cation-based semiconductors beyond lead halide perovskites for optoelectronic applications, *Adv. Mater.* 33 (2021) 2008574.
- 29 H. Huang, B. Pradhan, J. Hofkens, M.B.J. Roeflaers, J.A. Steele, Solar-driven metal halide perovskite photocatalysis: design, stability, and performance, *ACS Energy Lett.* 5 (2020) 1107–1123.
- 30 Z. Liu, H. Yang, J. Wang, Y. Yuan, K. Hills-Kimball, T. Cai, P. Wang, A. Tang, O. Chen, Synthesis of lead-free $\text{Cs}_2\text{AgBiX}_6$ ($X = \text{Cl}, \text{Br}, \text{I}$) double perovskite nanoplatelets and their application in CO_2 photocatalytic reduction, *Nano Lett.* 21 (2021) 1620–1627.
- 31 J. Pan, X. Li, X. Gong, J. Yin, D. Zhou, L. Sinatra, R. Huang, J. Liu, J. Chen, I. Dursun, A.M. El-Zohry, M.I. Saidaminov, H.-T. Sun, O.F. Mohammed, C. Ye, E. H. Sargent, O.M. Bakr, Halogen vacancies enable ligand-assisted self-assembly of perovskite quantum dots into nanowires, *Angew. Chem. Int. Ed.* 58 (2019) 16077–16081.
- 32 D.P. Nenon, K. Pressler, J. Kang, B.A. Koscher, J.H. Olshansky, W.T. Osowiecki, M. A. Koc, L.-W. Wang, A.P. Alivisatos, Design principles for trap-free CsPbX_3 nanocrystals: enumerating and eliminating surface halide vacancies with softer lewis bases, *J. Am. Chem. Soc.* 140 (2018) 17760–17772.
- 33 F. Wang, T. Hou, X. Zhao, W. Yao, R. Fang, K. Shen, Y. Li, Ordered macroporous carbonous frameworks implanted with CdS quantum dots for efficient photocatalytic CO_2 reduction, *Adv. Mater.* 33 (2021) 2102690.
- 34 T. Ouyang, H.-H. Huang, J.-W. Wang, D.-C. Zhong, T.-B. Lu, A dinuclear cobalt cryptate as a homogeneous photocatalyst for highly selective and efficient visible-light driven CO_2 reduction to CO in $\text{CH}_3\text{CN}/\text{H}_2\text{O}$ solution, *Angew. Chem. Int. Ed.* 56 (2017) 738–743.
- 35 J. Pal, S. Manna, A. Mondal, S. Das, K.V. Adarsh, A. Nag, Colloidal synthesis and photophysics of $\text{M}_3\text{Sb}_2\text{I}_9$ ($\text{M}=\text{Cs}$ and Rb) nanocrystals: lead-free perovskites, *Angew. Chem. Int. Ed.* 56 (2017) 14187–14191.
- 36 M. Xiao, Z. Wang, M. Lyu, B. Luo, S. Wang, G. Liu, H.-M. Cheng, L. Wang, Hollow nanostructures for photocatalysis: advantages and challenges, *Adv. Mater.* 31 (2019) 1801369.
- 37 Y. Yang, S. Zhao, F. Bi, J. Chen, Y. Li, L. Cui, J. Xu, X. Zhang, Oxygen-vacancy-induced O_2 activation and electron-hole migration enhance photothermal catalytic toluene oxidation, *Cell Rep. Phys. Sci.* 3 (2022), 101011.
- 38 K. Takanaka, Photocatalytic water splitting: quantitative approaches toward photocatalyst by design, *ACS Catal.* 7 (2017) 8006–8022.
- 39 W. Shangguan, Q. Liu, Y. Wang, N. Sun, Y. Liu, R. Zhao, Y. Li, C. Wang, J. Zhao, Molecular-level insight into photocatalytic CO_2 reduction with H_2O over Au nanoparticles by interband transitions, *Nat. Commun.* 13 (2022) 3894.
- 40 W. De Gruijter, J. Kerssen, EPR and luminescence of u.v. irradiated PbCl_2 and PbBr_2 crystals, *Solid State Commun.* 10 (1972) 837–841.
- 41 X. Li, Y. Sun, J. Xu, Y. Shao, J. Wu, X. Xu, Y. Pan, H. Ju, J. Zhu, Y. Xie, Selective visible-light-driven photocatalytic CO_2 reduction to CH_4 mediated by atomically thin CuIn_5S_8 layers, *Nat. Energy* 4 (2019) 690–699.
- 42 J. Di, J. Xia, M.F. Chisholm, J. Zhong, C. Chen, X. Cao, F. Dong, Z. Chi, H. Chen, Y.-X. Weng, J. Xiong, S.-Z. Yang, H. Li, Z. Liu, S. Dai, Defect-tailoring mediated electron-hole separation in single-unit-cell $\text{Bi}_3\text{O}_4\text{Br}$ nanosheets for boosting photocatalytic hydrogen evolution and nitrogen fixation, *Adv. Mater.* 31 (2019) 1807576.
- 43 Y. Zhang, Y. Zhang, H. Zhang, L. Bai, L. Hao, T. Ma, H. Huang, Defect engineering in metal sulfides for energy conversion and storage, *Coord. Chem. Rev.* 448 (2021), 214147.
- 44 Y. Dong, K. Li, W. Luo, C. Zhu, H. Guan, H. Wang, L. Wang, K. Deng, H. Zhou, H. Xie, Y. Bai, Y. Li, The role of surface termination in halide perovskites for efficient photocatalytic synthesis, *Angew. Chem. Int. Ed.* 59 (2020) 12931–12937.
- 45 X. Zou, Y. Zhao, X. Li, R. Chen, W. Shao, Z. Wang, J. Hu, J. Zhu, Y. Pan, Y. Sun, Y. Xie, Ultrastable and efficient visible-light-driven CO_2 reduction triggered by regenerative oxygen-vacancies in $\text{Bi}_2\text{O}_2\text{CO}_3$ nanosheets, *Angew. Chem. Int. Ed.* 60 (2021) 13840–13846.
- 46 H. Li, C. Cheng, Z. Yang, J. Wei, Encapsulated CdSe/CdS nanorods in double-shelled porous nanocomposites for efficient photocatalytic CO_2 reduction, *Nat. Commun.* 13 (2022) 6466.
- 47 P. Zhou, I.A. Navid, Y. Ma, Y. Xiao, P. Wang, Z. Ye, B. Zhou, K. Sun, Z. Mi, Solar-to-hydrogen efficiency of more than 9% in photocatalytic water splitting, *Nature* 613 (2023) 66–70.
- 48 Z. Miao, Q. Wang, Y. Zhang, L. Meng, X. Wang, In situ construction of S-scheme AgBr/BiOBr heterojunction with surface oxygen vacancy for boosting photocatalytic CO_2 reduction with H_2O , *Appl. Catal. B-Environ.* 301 (2022), 120802.
- 49 D. Voiry, H.S. Shin, K.P. Loh, M. Chhowalla, Low-dimensional catalysts for hydrogen evolution and CO_2 reduction, *Nat. Rev. Chem.* 2 (2018) 0105.
- 50 J. Bisquert, A. Zaban, M. Greenshtein, I. Mora-Sero, Determination of rate constants for charge transfer and the distribution of semiconductor and electrolyte electronic energy levels in dye-sensitized solar cells by open-circuit photovoltage decay method, *J. Am. Chem. Soc.* 126 (2004) 13550–13559.
- 51 C. Mao, F. Zuo, Y. Hou, X. Bu, P. Feng, In situ preparation of a Ti^{3+} self-doped TiO_2 film with enhanced activity as photoanode by N_2H_4 reduction, *Angew. Chem. Int. Ed.* 53 (2014) 10485–10489.

[52] Y. Kim, J.G. Smith, P.K. Jain, Harvesting multiple electron–hole pairs generated through plasmonic excitation of Au nanoparticles, *Nat. Chem.* 10 (2018) 763–769.

[53] S.S. Bhosale, A.K. Kharade, E. Jokar, A. Fathi, S.-M. Chang, E.W.-G. Diau, Mechanism of photocatalytic CO_2 reduction by bismuth-based perovskite nanocrystals at the gas-solid interface, *J. Am. Chem. Soc.* 141 (2019) 20434–20442.

[54] F. Hu, L. Yang, Y. Jiang, C. Duan, X. Wang, L. Zeng, X. Lv, D. Duan, Q. Liu, T. Kong, J. Jiang, Y. Xiong, Ultrastable Cu catalyst for CO_2 electroreduction to multicarbon liquid fuels by tuning C–C coupling with CuTi subsurface, *Angew. Chem. Int. Ed.* 60 (2021) 26122–26127.

[55] S. Rousseau, O. Marie, P. Bazin, M. Daturi, S. Verdier, V. Harlé, Investigation of methanol oxidation over Au/catalysts using operando IR spectroscopy: determination of the active sites, intermediate/spectator species, and reaction mechanism, *J. Am. Chem. Soc.* 132 (2010) 10832–10841.

[56] W. Zhong, Y. Liu, D. Zhang, Theoretical study of methanol oxidation on the PtAu (111) bimetallic surface: CO pathway vs non-CO pathway, *J. Phys. Chem. C* 116 (2012) 2994–3000.

[57] I. Palacio, J.M. Rojo, O. Rodriguez, de la Fuente, Surface defects activating new reaction paths: formation of formate during methanol oxidation on Ru(0001), *ChemPhysChem* 13 (2012) 2354–2360.